



HAL
open science

Deterministic control of ferroelectric polarization by ultrafast laser pulses

Peng Chen, Charles Paillard, Hong Jian Zhao, Jorge Íñiguez, Laurent Bellaïche

► **To cite this version:**

Peng Chen, Charles Paillard, Hong Jian Zhao, Jorge Íñiguez, Laurent Bellaïche. Deterministic control of ferroelectric polarization by ultrafast laser pulses. *Nature Communications*, 2022, 13 (1), pp.2566. 10.1038/s41467-022-30324-5 . hal-03664634

HAL Id: hal-03664634

<https://centralesupelec.hal.science/hal-03664634>

Submitted on 11 May 2022

HAL is a multi-disciplinary open access archive for the deposit and dissemination of scientific research documents, whether they are published or not. The documents may come from teaching and research institutions in France or abroad, or from public or private research centers.

L'archive ouverte pluridisciplinaire **HAL**, est destinée au dépôt et à la diffusion de documents scientifiques de niveau recherche, publiés ou non, émanant des établissements d'enseignement et de recherche français ou étrangers, des laboratoires publics ou privés.

Deterministic control of ferroelectric polarization by ultrafast laser pulses

Peng Chen,¹ Charles Paillard,² Hong Jian Zhao,^{1,3} Jorge Íñiguez,^{4,5} and L. Bellaiche¹

¹*Physics Department and Institute for Nanoscience and Engineering,
University of Arkansas, Fayetteville, Arkansas 72701, USA*

²*Laboratoire Structures, Propriétés et Modélisation des Solides, CentraleSupélec,
UMR CNRS 8580, Université Paris-Saclay, 91190, Gif-sur-Yvette, France*

³*International Center for Computational Method and Software (ICCMS),
Jilin University, 2699, Qianjin Street, Changchun, 130012, China*

⁴*Materials Research and Technology Department,
Luxembourg Institute of Science and Technology (LIST),*

Avenue des Hauts-Fourneaux 5, L-4362 Esch/Alzette, Luxembourg

⁵*Physics and Materials Science Research Unit, University of Luxembourg, 41 Rue du Brill, L-4422 Belvaux, Luxembourg*

(Dated: October 14, 2021)

Ultrafast light-matter interactions present a promising route to control ferroelectric polarization at room temperature, which is an exciting idea for designing novel ferroelectric-based devices. One emergent light-induced technique for controlling polarization consists in anharmonically driving a high-frequency phonon mode through its coupling to the polarization. A step towards such control has been recently accomplished, but the polarization has been reported to be only *partially* reversed and for a short lapse of time. Such transient partial reversal is not currently understood, and it is presently unclear if a full control of polarization, by, e.g., fully reversing it or even making it adopt different directions (thus inducing structural phase transitions), can be achieved by activating the high-frequency phonon mode via terahertz pulse stimuli. Here, by means of realistic simulations of a prototypical ferroelectric, we reveal and explain (1) why a transient partial reversal has been observed, and (2) how to deterministically control the ferroelectric polarization thanks to these stimuli. Such results can provide guidance for realizing original ultrafast optoferroic devices.

Introduction

Manipulation of properties of quantum materials utilizing (GHz-THz) high-frequency light is a fascinating topic in modern solid-state physics¹⁻⁶. It has resulted in several breakthroughs in the past decade. Examples include stimulating insulator-metal transitions^{7,8}, controlling magnetic domains⁹⁻¹³, uncovering hidden phases¹⁴⁻¹⁷, inducing superconductivity¹⁸⁻²¹ as well as the formation of photon-dressed topological states²²⁻²⁴. Light-induced switching of ferroelectric polarization²⁵⁻³⁴ is also among these most important achievements since it can result in novel optoferroic devices, especially ultrafast nonvolatile ferroelectric memories^{35,36}.

In particular, recent works proposed and demonstrated that the ferroelectric polarization can be reversed by exciting a high-frequency infrared-active phonon mode (to be denoted as auxiliary mode or auxiliary high-frequency mode in the following) that is coupled to the soft mode (which is mostly associated with this polarization), with this effect acting through an intermediate anharmonic driving force^{29,37,38}. Such indirect method stimulates coherent phonon modes and has the potential to achieve polarization switching within a few hundred femtosecond, which will be six orders of magnitude faster than from photovoltaic effects^{27,28,39}. This route was first theoretically proposed by A. Subedi and his coworkers³⁸ and then partially realized by Mankowsky *et al.* in their second harmonic generation (SHG) experiment²⁹.

However, some experimental results contradict predictions from the theory. For instance, the model of Ref. [38]

predicted a full reversal of the polarization while measurements “only” reported a transient reversal^{26,29}, with the reversed polarization not even reaching its equilibrium value. It is presently unclear why only a partial transient reversal was observed²⁹ and whether it is, in fact, possible to achieve a full reversal. Possible reasons for such paucity of knowledge is that the theory of Ref. [38] may have missed important couplings⁴⁰. Moreover, the fact that the studied model of Ref. [38] is only one-dimensional in nature also implies that some striking features may have been overlooked, especially in systems that can adopt polarization along different crystallographic directions. For instance, is it possible to make the polarization rotate rather than reverse by activating an auxiliary high-frequency mode? Can we also expect novel effects when applying such light-induced indirect method to different structural phases, each having its own direction for the ferroelectric polarization, such as rhombohedral, orthorhombic and tetragonal states in ferroelectric perovskites?

The aim of the present study is to answer all these questions by employing an original atomistic scheme that includes the three-dimensional soft mode, the three-dimensional auxiliary high-frequency mode and all their relevant couplings. As we will see, this atomistic approach not only reproduces a transient partial reversal analogous to the one observed in the experiments of Ref. [29], but also provides insight into the light-driven effects. It further reveals and explains how a full reversal (180° rotation) can indeed happen in some cases; and

also predict a variety of light-induced phase transitions, for which polarization rotates by 60° , 71° , 90° , and 109° , as a result of a mechanism we coin here as “squeezing”. The discovery of such “squeezing” mechanism further allows us to design a strategy for an ultrafast deterministic control of the polarization and even realize full-reversal in a deterministic manner.

Results

As we are looking for an universal behavior of the THz response of the resonated auxiliary high-frequency mode and its consequence on electrical polarization, the prototypical ferroelectric material KNbO_3 is chosen. **It allows us to explore different ferroelectric phases with different polarization’s directions at different temperature, which leads to a richer playground that one-dimensional ferroelectrics (e.g. LiNbO_3) or tetragonal ferroelectrics (e.g., PbTiO_3 that has only a single transition from cubic with no polarization to tetragonal with a polarization along $\langle 001 \rangle$).** A novel effective Hamiltonian, H_{eff} , is developed for such system, and is detailed in the method section. Its degrees of freedom are vectors related to the ferroelectric soft mode (\mathbf{P}), high-frequency auxiliary mode (\mathbf{Q}) which is polar as well, and inhomogeneous strain (\mathbf{u}) in each 5-atom unit cell, as well as, the homogenous strain (η) affecting the whole simulation supercell. **Such effective Hamiltonian does not explicitly include electronic degrees of freedom but rather takes into the ionic displacements associated with the \mathbf{Q} and \mathbf{P} modes.** Note that this model is similar to previous effective Hamiltonians for ferroelectric perovskites⁴¹, except for the explicit consideration of the high-frequency polar mode \mathbf{Q} and its couplings. **Note also that, in our light-matter interaction model, only the TO modes of both the soft \mathbf{P} mode and high-frequency \mathbf{Q} mode are incorporated (with these two types of TO modes being coupled to each other).**

Phase diagram. Before studying the behavior of the ferroelectric polarization under a mid-infrared pulse, let us first explore the phase diagram of KNbO_3 by running Monte Carlo (MC) simulations using our first-principle-based effective Hamiltonian on a $12 \times 12 \times 12$ supercell. Figures 1 (a) and 1 (b) report the temperature behavior of the three Cartesian components of the supercell average of the \mathbf{P} and \mathbf{Q} modes, respectively. These figures indicate that our model can nicely reproduce the sequence of phase transitions observed in **experiments**, that is, from cubic to tetragonal (for which a large P_z coexists with a small Q_z), then from tetragonal to orthorhombic (where both P_y and Q_y get activated and become equal to P_z and Q_z , respectively) and finally from orthorhombic to rhombohedral (for which we have now large $P_x = P_y = P_z$ and small $Q_x = Q_y = Q_z$), when cooling down the system. Note that \mathbf{P} and \mathbf{Q} are of opposite sign for the tetragonal (T), orthorhombic (O) and rhombohedral (R) phases, as a direct consequence of the positive signs of some coupling parameters indicated in Table I and further discussed later on. Examples of predicted values for the total polarization for R, O, and T phases are $54 \mu\text{C}/\text{cm}^2$ at 10 K, $48 \mu\text{C}/\text{cm}^2$ at 300

K and $42 \mu\text{C}/\text{cm}^2$ at 400 K. They compare reasonably well with the experimental values of $42 \pm 4 \mu\text{C}/\text{cm}^2$, $32 \pm 3 \mu\text{C}/\text{cm}^2$ and $30 \pm 2 \mu\text{C}/\text{cm}^2$ that one can find at at 230 K, 370 K and 473 K in these three phases, respectively, in Refs. [42, 43]. However as is often the case with effective Hamiltonians⁴⁴, some predicted transition temperatures are lower than the experimental ones⁴³, namely **640 K versus 708 K** for the C-to-T transition, and **345 K versus 498 K** for the T-to-O transition. On the other hand, the R-to-O transition temperature is well reproduced here: **260 K** for the effective Hamiltonian and 263 K in measurements. Interestingly, we also numerically found that, if the \mathbf{Q} degrees of freedom are turned off, the O-phase vanishes and only two phase transitions occur: one from T-to-C at a lower temperature around 500 K and a second one from R-to-T around 400 K. Such fact highlights the importance of incorporating both \mathbf{P} and \mathbf{Q} in order to accurately model properties of KNbO_3 . Note, however, that a previous model without \mathbf{Q} did find an O equilibrium phase, but for some narrow temperature range ($\simeq 50$ K)⁴⁵. One can also easily imagine the development of a model having \mathbf{P} as the only polar degree of freedom, but where the effect of \mathbf{Q} would be to renormalize the coefficients associated with \mathbf{P} .

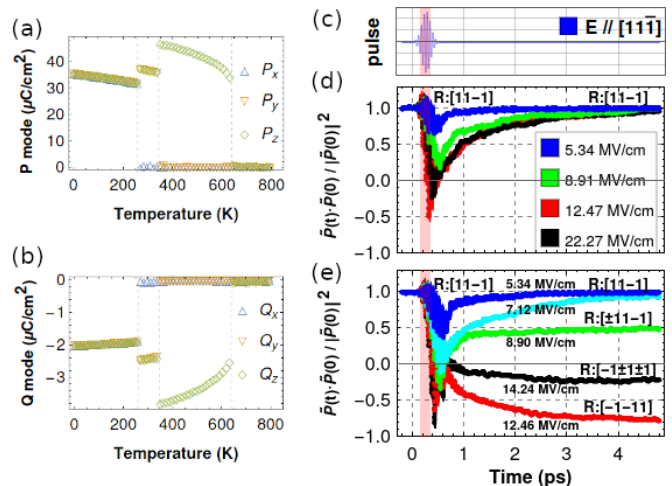


FIG. 1. Results to be compared with experiments: \mathbf{P} (a) and \mathbf{Q} (b) modes as a function of temperature; Ratio involving the total polarization at 240K as a function of time, for partial-excitation (d) and full-excitation (e) starting from a R phase. Panel (c) shares the same horizontal axes with Panels (d) and (e) to indicate the laser pulse shape and time evolution. Pink regions are to indicate the full-width-half-maximum of the Gaussian enveloped laser pulse.

Electrical polarization reversal. Let us now check if the presently developed method also allows to reproduce a situation similar to the one reported in Ref. [29], namely, an electrical polarization transient reversal in a rhombohedral state of a ferroelectric material. For that, we employ the aforementioned H_{eff} within Molecular Dynamics (MD) simulations on a R-phase of KNbO_3 at 240 K, for which \mathbf{P} is along $[11\bar{1}]$ and \mathbf{Q} antiparal-

179 lel to it. Technically and in order to be close to the
 180 experimental situation of Ref. [29], we mimic the appli-
 181 cation of a ‘‘Gaussian enveloped’’ laser pulse of the form
 182 $\mathbf{E}e^{-2\ln 2(\frac{t}{\tau})^2}\cos(2\pi\omega t)$ (with a full-width-half-maximum
 183 (FWHM) $\tau = 200$ fs and frequency $\omega = 18$ THz) and
 184 a light polarization (\mathbf{E}) which is parallel to $[11\bar{1}]$. Note
 185 also that, as detailed in Sec. I of the Supplementary Ma-
 186 terial (SM), this 18 THz frequency is chosen here because
 187 it is close to the resonance of the high-frequency auxil-
 188 iary mode, while the frequency of the soft-mode is found
 189 to be $\simeq 8$ THz at 240K, according to our calculations.
 190 In order to further compare with the measurements of
 191 Ref. [29], the dot product of the total polarization at
 192 time t , $\tilde{\mathbf{P}}(t) = \mathbf{P}(t) + \mathbf{Q}(t)$, and its initial value, $\tilde{\mathbf{P}}(0)$,
 193 is calculated and then divided by the square of $|\tilde{\mathbf{P}}(0)|$
 194 for different magnitudes of the electric field and with the
 195 pulse starting at $t=0$ ps. Note that, in simulations with
 196 this type of effective models, the applied electric fields
 197 are typically predicted to be 20 times larger than the ex-
 198 perimental ones⁴⁶. The results are shown in fig. 1 (d). As
 199 only a fraction of the material was excited in the exper-
 200 iment (done on a 5 mm thick LiNbO₃ sample), we also
 201 assumed that only a portion of our supercell is experi-
 202 encing the pulse (technically, only 10x10x10 cells within
 203 the 12x12x12 supercell are allowed to be coupled to the
 204 electric field) and keep the homogenous strains fixed at
 205 its initial values to mimic clamping. Only the dipoles
 206 subject to the pulse are incorporated in the computation
 207 of $\tilde{\mathbf{P}}(0)$ and $\tilde{\mathbf{P}}(t)$.

208 One can see that, for small magnitude of the electric
 209 field associated to the pulse, e.g., 5.34 MV/cm, the po-
 210 larization (blue curve in fig. 1 (d)) first decreases from
 211 its initial value, while still being along $[11\bar{1}]$, before in-
 212 creasing and desiring to reach $\tilde{\mathbf{P}}(0)$ again at larger times.
 213 The dip in polarization is enhanced when increasing the
 214 magnitude of the field to 8.91 MV/cm (green curve in
 215 fig. 1 (d)) until such dip becomes negative for 12.47
 216 MV/cm (red curve in fig. 1 (d)). In other words, for
 217 strong enough pulses, the total polarization $\tilde{\mathbf{P}}$ has been
 218 reversed when activating the high-frequency auxiliary
 219 mode, exactly like in the measurements of Ref. [29]. As
 220 similar to these experiments too, this reversal is partial
 221 (*i.e.*, the ratio shown in fig. 1 (d) never reaches
 222 -1) and is transient in nature, since the polarization
 223 becomes positive again and approaches $\tilde{\mathbf{P}}(0)$ at longer
 224 times. Note that, in our present case, the full recovery
 225 to its initial values of $\tilde{\mathbf{P}}(t)$ happens at larger times than
 226 in Ref. [29], which is likely due to some material speci-
 227 ficity. For instance, the system studied there is LiNbO₃
 228 rather than KNbO₃, and thus possesses strong oxygen
 229 octahedral rotations that have the tendency to interact
 230 with polarization^{47–50}. On a microscopic level, we found
 231 that the dip of the red curve is caused by local dipoles
 232 subject to the pulse being aligned along the reverse $[\bar{1}\bar{1}\bar{1}]$
 233 direction or deviating away from the original $[11\bar{1}]$ direc-
 234 tion.

235 Furthermore, Ref. [29] also suggested that with an even

236 stronger laser pulse (out of their laser device’s reach) a
 237 full reversal would have been achieved. However, our nu-
 238 merical simulation (black in fig. 1 (d)) shows that this is
 239 not the case. As a matter of fact, with laser pulses up
 240 to 22.27 MV/cm, this full-reversal never happened, but
 241 rather the ratio shown in fig. 1 (d) gets close to zero be-
 242 fore $\tilde{\mathbf{P}}(t)$ increases towards $\tilde{\mathbf{P}}(0)$. One may wonder if this
 243 lack of full reversal stems from the fact that only a part
 244 of the sample is excited for the results of fig. 1 (d). To
 245 check such possibility, fig. 1 (e) reports the correspond-
 246 ing predictions but when the whole system is subject to
 247 the same aforementioned pulse. Note that since we do
 248 not expect clamping from a non-excited part of the ma-
 249 terial, we now allow the homogeneous strains to relax.
 250 The polarization can indeed be fully reversed within a R-
 251 phase by a field of 12.46 MV/cm magnitude (red curve).
 252 However, not like previously expected^{29,38}, the full re-
 253 versal does not happen during the pulse but after. In
 254 addition, we numerically find that the polarization can
 255 also reach a final state where it points along a direction
 256 oblique to $[11\bar{1}]$. For instance, an electric field of $E=8.90$
 257 MV/cm gives rise to a final state with half of the material
 258 presenting polarization along the rotated $[\bar{1}\bar{1}\bar{1}]$ direction
 259 (71° rotation) and with the other half still along the ini-
 260 tial $[11\bar{1}]$ direction (green curve in fig. 1 (e)). Similarly,
 261 a larger electric field $E=14.24$ MV/cm induces a polar-
 262 ization being now along other directions, namely $[\bar{1}\bar{1}\bar{1}]$
 263 (109° rotation), $[\bar{1}\bar{1}\bar{1}]$ (71° rotation), and $[\bar{1}\bar{1}\bar{1}]$ (180° ro-
 264 tation), black curve in fig. 1 (e), in different parts of
 265 the material at the end. This explains why the ratio of
 266 fig. 1 (e) is equal to 0.5 and -0.2 for $E=8.90$ MV/cm and
 267 $E=14.24$ MV/cm, respectively. Details of the evolution
 268 of each of the polarization components can be found in
 269 sec. III of SM. The results of fig. 1 (e) therefore reveal
 270 that rotation of polarization in a ferroelectric perovskite,
 271 rather than ‘‘only’’ its reversing, have also to be consid-
 272 ered and understood, when subjecting a ferroelectric to a
 273 high-frequency electric field. Our results so far show that
 274 having a three-dimensional ferroelectric like KNbO₃ al-
 275 lows a wide range of possibilities for polarization control.
 276 Clearly, having a three-dimensional model of the interac-
 277 tions between \mathbf{P} and \mathbf{Q} in this case is essential. We now
 278 focus on simple cases, such as T- and O-phases under
 279 pulses, to explore and understand such possibilities.

280 **Squeezing effect.** Let us thus take a T-phase at 400 K
 281 with a polarization lying along the positive z-direction,
 282 with all the degree of freedoms being allowed to evolve
 283 (e.g., \mathbf{P} , \mathbf{Q} , inhomogeneous and homogeneous strains),
 284 as a simple case. We assume that the whole system is
 285 excited by a laser pulse $\mathbf{E}e^{-2\ln 2(\frac{t}{\tau})^2}\cos(2\pi\omega t)$, for which
 286 $\tau = 600$ fs, $\omega = 19$ THz and \mathbf{E} is applied along the z-
 287 direction with a magnitude of 7.71 MeV/cm, as depicted
 288 in fig. 2 (a). Such pulse naturally leads to Q_z resonating,
 289 as evidenced in fig. 2 (b). Within the full-width-half-
 290 maximum (600 fs rather than 200 fs in order to have
 291 more oscillations of some components of \mathbf{Q} around zero)
 292 of the pulse, two striking features emerge and are seen in
 293 fig. 2 (c): 1) P_z decreases its absolute value to zero, and

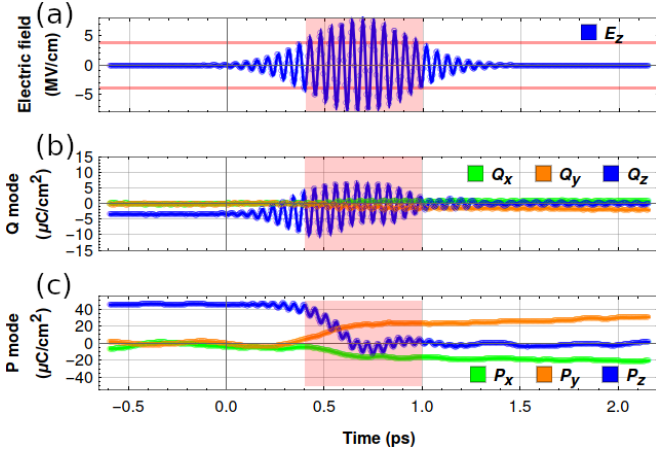


FIG. 2. **Squeezing effect in T-phase:** Temporal behavior of the **Q** (b) and **P** (c) modes at 400K, as a response to the electric field’s pulse shown in (a) and when starting from a T-phase (note that the full-width-half-maximum of the pulse is marked by pink regions).

2) P_x and P_y adopt non-zero values (with negative and positive sign, respectively). Consequently, P_z does *not* reverse itself after going through zero. It rather keeps oscillating around zero, which means that when the polarization is at a zero value the reversal driving force as predicted in Refs. [29, 38] vanishes and stops to push P_z towards the opposite direction. After the pulse has occurred, the system chooses a O-phase with a polarization along the $[\bar{1}10]$ direction (90° rotation) – via the creation of x- and y-components and P_z continuing to be around zero. (Such O-phase in some of our simulations will further transform back to another T-phase, such as those with a polarization along $[\bar{1}00]$ or $[010]$, while in other simulations this O-phase will have a longer life time at 400 K.) The applied pulse therefore **would prefer to annihilate** the component of the polarization that is along the field’s direction, in favor of polarization’s components that are perpendicular to the field. The mid-infrared pulse thus acts like a “squeezer” that “presses” the material along the pulse polarized direction **and reduces the magnitude of the component of the polarization that is along the field**. To demonstrate that the direct coupling between electric field and **P** mode is not the reason that **P** is squeezed, we ran a numerical experiment in which the degree of freedoms of the **P** mode, inhomogeneous and homogeneous strains are allowed to evolve while the **Q** mode is kept frozen to its equilibrium initial value. In that case, no squeezing effect was observed and P_z was “only” oscillating around its equilibrium value in the initial T-phase instead of being annihilated (see sec. IV of SM). The activation and response of the **Q** mode to the pulse are therefore required to induce the squeezing effect of **P**.

To understand such squeezing effect, we need to have a detailed look at Table I and realize that, for the case of a T-phase having a z-component of the polarization, the

TABLE I. On-site couplings between ferroelectric soft mode **P** and high-frequency auxiliary mode **Q**. The unit of these fourth-order coupling coefficients is Nm^6/C^4 .

Coefficients (Λ)	Coupling Energies
2.02×10^{13}	$\Lambda_2(P_x^2 Q_x^2 + P_y^2 Q_y^2 + P_z^2 Q_z^2)$
-2.13×10^{12}	$\Lambda_{22}(P_x^2 Q_y^2 + P_x^2 Q_z^2 + P_y^2 Q_z^2 + P_y^2 Q_x^2 + P_z^2 Q_x^2 + P_z^2 Q_y^2)$
2.68×10^{11}	$\Lambda_3(P_x^3 Q_x + P_y^3 Q_y + P_z^3 Q_z)$
8.86×10^{11}	$\Lambda_1(P_x Q_x^3 + P_y Q_y^3 + P_z Q_z^3)$
9.69×10^{11}	$\Lambda_{211}(P_x^2 P_y Q_y + P_x P_y^2 Q_x + P_z^2 P_z Q_z + P_x P_z^2 Q_x + P_y^2 P_z Q_z + P_y P_z^2 Q_y)$
-4.61×10^{11}	$\Lambda_{112}(P_x Q_x Q_y^2 + P_y Q_x^2 Q_y + P_z Q_x^2 Q_z + P_x Q_x Q_z^2 + P_z Q_y^2 Q_z + P_y Q_y Q_z^2)$
1.70×10^{13}	$\Lambda_{1111}(P_x P_y Q_x Q_y + P_y P_z Q_y Q_z + P_z P_x Q_z Q_x)$

following couplings are relevant: the bi-quadratic

$$U_{22}^{(z)} = \Lambda_2 P_z^2 Q_z^2 \quad (1)$$

$$U_{22}^{(x-z)} = \Lambda_{22}(P_x^2 + P_y^2) Q_z^2 \quad (2)$$

When a mid-infrared laser pulse polarized along z is applied, the high-frequency auxiliary mode Q_z resonates with a large amplitude. The positive $U_{22}^{(z)}$ interaction (see Table I for its coefficient Λ_2) then gives rise to a large positive quadratic term $\Lambda_2 Q_z^2 P_z^2$ felt by P_z . Let us understand the consequence of such large positive term on the polarization, by considering a fourth-order model for the free energy, namely $F = \alpha P_z^4 - \kappa^2 P_z^2 + \Lambda Q_z^2 P_z^2$. The polarization can thus have two minima (hence a double well potential), that are $P_z^\pm = \pm \sqrt{(\kappa^2 - \Lambda Q_z^2)/(2\alpha)}$ (note that α is always positive to have a bounded energy potential). If Λ is positive and $\kappa^2 - \Lambda Q_z^2 > 0$, the equilibrium value of P_z shrinks in magnitude (and the double well potential becomes shallower) when Q_z^2 is growing. Such double well can even transform into a single well with its minimum at $P_z = 0$, when $\kappa^2 - \Lambda Q_z^2$ becomes negative. The wiggly decreasing-in-magnitude of P_z to zero in fig. 2 (c) within the full-width-half-maximum of the pulse, corresponds to the oscillation of P_z within a shrinking double-well potential. Moreover, the growing of P_x and P_y in fig. 2 (c) within the full-width-half-maximum of the pulse is favored by the fact that $U_{22}^{(x-z)}$ has a negative coefficient Λ_{22} in front of it and becomes stronger when Q_z^2 is enlarged through its resonance. Considering that usually the crossing term Λ_{22} is much smaller than Λ_2 (one order of magnitude smaller), the decreasing of the polarization component that parallels to the field should be dominant over the increasing of the perpendicular component. Note that the squeezing effect decides along which direction the polarization should be induced but not the sign of this polarization. For instance, the final result at 2 ps of fig. 2(c) for the axis for which **P** is parallel to could also have been $[110]$, $[\bar{1}\bar{1}0]$, or $[\bar{1}\bar{1}0]$. Note too that we have also performed various numerical experiments such, as, e.g., switching in and off some interactions in the simulations, that con-

firm the role of $U_{22}^{(z)}$ and $U_{22}^{(x-z)}$ on the aforementioned effects. It is also realized that the Λ_3 and Λ_1 couplings in Table I decide the direction of the \mathbf{Q} mode with respect to that of the \mathbf{P} mode, details can be found in sec. IV of SM.

It is worthwhile to emphasize that this squeezing effect is a new phenomenon that originates from the high-frequency auxiliary mode. It should not be accounted as the reduction of the polarization by the thermal effect from the light^{51–53} because fig. 2 clearly shows that though one component (P_z) decreased to zero, other components (P_x and P_y) condense along with it, while heating will typically result in a reduction of the polarization magnitude overall.

This squeezing effect also allows us to understand the results about partial (transient) and full (permanent) reversal of polarization in fig. 1 (d) and (e) for some fields within a R-phase. As a matter of fact, pulses with fields oriented along the $[1\bar{1}\bar{1}]$ axis and with the resonant 18 THz frequency induce a strong oscillation of the \mathbf{Q} mode along such $[1\bar{1}\bar{1}]$ axis within the R-phase. During the large oscillation of \mathbf{Q} (and resulting large Q_x^2 , Q_y^2 and Q_z^2), the \mathbf{P} mode starts to decrease its magnitude towards zero according to the squeezing mechanism along all three Cartesian directions. After the exit of the 200 fs full-width-half-maximum pulse, \mathbf{P} has just reached and oscillated around zero with net momentum towards the reverse $[\bar{1}\bar{1}\bar{1}]$ direction. If it is a full-excitation case (fig. 1 (e), in which all unit cells are subject to the electric field), \mathbf{P} can continue to grow along the $[\bar{1}\bar{1}\bar{1}]$ direction and the full reversal of the polarization then occurs. If it is a partial-excitation case (fig. 1 (d), in which 10x10x10 cells within the 12x12x12 supercell are allowed to be coupled to the electric field), \mathbf{P} can partially grow along $[\bar{1}\bar{1}\bar{1}]$ but then quickly reverses its direction and grows back to $[1\bar{1}\bar{1}]$, as a result of the interaction with the unexcited part of the material; the transient partial reversal of the polarization thus happens. We also note that Abalmasov⁵⁴ proposed that the depolarizing electric field can yield a similar transient partial reversal in thin films. Note that the Supplemental Materials also explain why the polarization can rotate, rather than being reverted, under full-excitation for some fields.

Deterministic full-reversal strategy. As can be seen in fig. 1 (e), the ferroelectric polarization full reversal is sometimes replaced by a polarization rotation. Consequently, a single laser pulse, such as the one used in the experiment of Ref. [29], will not reverse the polarization of a three-dimensional ferroelectric in a deterministic manner. (Presumably, the reversal will not be deterministic for a one-dimensional compound like LiNbO₃ either, unless one implements a way to avoid the back-switching to the original state.) However, the understanding of the squeezing effect can enable us to further design a strategy at room temperature to realize a full-reversal of the ferroelectric polarization by laser pulses aided with a tiny dc and constantly applied gate field, which is of high importance for building novel ferroelectric-based devices.

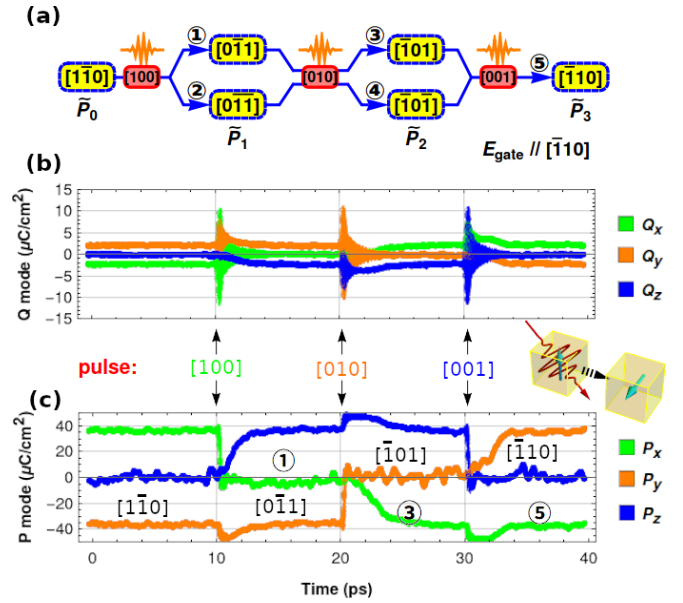


FIG. 3. **Deterministic full-reversal strategy:** (a) protocol of the three-pulse reversal process; the yellow background boxes are for the initial and excited polarization phases and the pink background boxes are used to indicate the laser pulses that are along x, y, and z-axis; The labels of the phases $\tilde{\mathbf{P}}$ is defined as $\mathbf{P} + \mathbf{Q}$ to indicate the total polarization; The blue arrows are used to indicate the phase transition channels after the laser pulses; Responses of the \mathbf{Q} (b) and \mathbf{P} modes (c) excited by a sequence of three “200fs-18THz” pulses activated at 10, 20, and 30 ps and having their polarized direction along $[100]$, $[010]$, and $[011]$ directions, respectively. For each of these pulses, the magnitude of \mathbf{E} in $\mathbf{E}e^{-2\ln 2(\frac{t}{\tau})^2} \cos(2\pi\omega t)$ is 6.17 MV/cm.

Then, we take advantage of the following expected features: (1) that the squeezing effect wants to suppress the component of the polarization that is aligned along the pulse’s direction; (2) when forming from a zero value, the components of the polarization will adopt the same sign as those of the applied weak dc field; and (3) the system wishes to stay in an O-phase due to the constant temperature of 300K (for which O-phases are the equilibrium state). We can thus anticipate, as displayed in fig. 3 (a), that (i) a first pulse applied along $[100]$ will lead to a new polarization, $\tilde{\mathbf{P}}_1$, being now either along $[0\bar{1}\bar{1}]$ (channel 1 in fig. 3 (a)) or $[0\bar{1}\bar{1}]$ (channel 2 in fig. 3 (a)); (ii) a second pulse but now applied along $[010]$ either transforms $\tilde{\mathbf{P}}_1$ being parallel to $[0\bar{1}\bar{1}]$ to $\tilde{\mathbf{P}}_2$ being along $[\bar{1}0\bar{1}]$ (channel 3 in fig. 3 (a)) or $\tilde{\mathbf{P}}_1$ being along $[0\bar{1}\bar{1}]$ to $\tilde{\mathbf{P}}_2$ being parallel to $[\bar{1}0\bar{1}]$ (channel 4 in fig. 3 (a)); and finally (iii) a third pulse, now along $[001]$ should lead to a $\tilde{\mathbf{P}}_3$ polarization along $[\bar{1}\bar{1}\bar{1}]$ (channel 5 in fig. 3 (a)) for the two possible $\tilde{\mathbf{P}}_2$ starting points (channels 3 and 4). If that is the case, we will thus have achieved a fully deterministic (3-pulse process) reversal of the polarization from the initial to final states. It is worth to mention that the use of several pulses is a common strategy to switch

ferroelectric polarization in deterministic manner⁵⁵ and has also been suggested by other theoretical work⁵⁶.

In figs. 3 (b) and (c), we present one representative of our many *numerical* examinations, in order to check our proposed strategy and to explain it in even more details. An equilibrium O-phase, having $P_x = -P_y > 0$, along with weak $Q_x = -Q_y < 0$, is thus chosen at room temperature (300 K) as the initial state. Three pulses are applied along different directions and at different times, along with a bias *dc* gate field constantly applied along the $[110]$ direction. The magnitude of this *dc* field is rather weak, namely 0.0154 MV/cm which is only 3.3% of the minimum *dc* field needed to reverse the O-phase polarization in our numerical model and about 0.35% of the magnitude of laser pulse to be applied. As indicated above, the role of this tiny *dc* field is to bias the *x* and *y*-components of \mathbf{P} to have negative and positive sign, respectively, when forming, since squeezing effects alone do not guarantee the *sign* of such components. Practically, a “200fs-18THz” laser pulse (i.e., a pulse with $\tau = 200$ fs and frequency $\omega = 18$ THz in $\mathbf{E}e^{-2ln2(\frac{t}{\tau})^2} \cos(2\pi\omega t)$) is first applied at 10 ps with $E=6.17$ MV/cm and along the $[100]$ direction on this O-phase having a polarization along the $[1\bar{1}0]$ direction (note that 18 THz is close enough to the resonant frequency of the auxiliary mode of the O-phase at 300 K). This pulse thus resonates with the auxiliary mode Q_x (see fig. 3 (b)), and, as expected by the squeezing effect, (i) the component of the polarization along the *x*-direction, P_x , vanishes, as shown in fig. 3 (c), and (ii) the *y*-axis along which there is no pulse field, sees its component of polarization, P_y , to remain finite and even to further grow in magnitude. Concomitantly, Q_y also slightly increases in its absolute value, because of its $\Lambda_3 P_y^3 Q_y$ and $\Lambda_1 P_y Q_y^3$ couplings with P_y . Since the minima of the free energy at 300 K are orthorhombic phase, while P_x is squeezed to zero, the P_z component develops and takes a positive value in this particular numerical experiment. Note that, beyond the fact that the material will try to adopt an O-phase at this temperature, the squeezing effect of the form $\Lambda_{22} P_z^2 Q_y^2$ (i.e., an equivalent form of eq. 2, but for P_z and Q_y) will also contribute to the development of P_z . Note also that, since no *dc* field is along the *z*-axis, the newly-formed P_z can also be negative, which corresponds to the channel ② in fig. 3 (a) and which we also observed in our other numerical experiments (see sec. V of SM). We have thus succeeded to make a transition from an O-phase to another O-phase (channel ①) at 300 K via a rotation of the polarization by 60° , by activating the auxiliary high-frequency mode at around 10 ps. The second pulse is also a “200fs-18THz” one with the same magnitude $E=6.17$ MV/cm, but now having a $[010]$ polarized orientation, which then, according again to the squeezing effect, results in the vanishing of the P_y (and also of Q_y) in favor of the activation of P_x (and also Q_x) that remains finite until 30 ps. The formation of P_x at 20 ps has the same origin as the formation of P_z at 10 ps, but the P_x now has to adopt negative sign because of the small *dc* field’s component along

$[\bar{1}00]$. Another O-phase with polarization along $[\bar{1}01]$ has therefore been created, corresponding to the channel ③ in fig. 3 (a). Similarly, a third “200fs-18THz” pulse with the same magnitude $E=6.17$ MV/cm is applied at 30 ps, but with a pulse field now oriented along $[001]$. Consequently, squeezing effects lead to P_y now becoming finite (and positive thanks to the gate field) while P_z vanishes, and P_x remains negative. An O-phase, but now with a polarization fully reversed with respect to the initial O-phase, has thus formed.

The strategy of fig. 3 therefore allows to realize a full-reversal of polarization in a deterministic fashion, via three steps each taking advantage of the squeezing effects (which eliminate the polarization component that is parallel to the pulse polarization direction, while inducing the formation of the polarization along the perpendicular directions) combined with the application of a weak *dc* field that controls the sign of the newly formed component of the polarization. Section V of the SM further provides details on this deterministic control by showing results of the different paths indicated in fig. 3 (a), when changing the magnitude of the laser pulses. It is also worth to mention that a deterministic rotation of the polarization by 60° is obviously possible. For instance, if the weak *dc* bias field is applied along $[001]$, a single *x*-polarized pulse will deterministically transform an O-phase with a polarization along $[110]$ phase to another O-phase but with a polarization along $[011]$ at room temperature in KNbO₃.

In conclusion, we developed a method that allows to model the pulse stimuli on the ferroelectric polarization by resonating an auxiliary high-frequency mode, taking the prototypical ferroelectric material KNbO₃ as a testbed. Our study has revealed and explained how one can obtain a partial transient ferroelectric polarization reversal in SHG experiments, shedding light on the results of Ref. [29]. We also show that, and explain why, a full reversal of the polarization, as well as phase transitions induced by rotation of the polarization, can occur as a response to different polarized laser pulses activating different Cartesian components of the auxiliary mode. We hope the mechanisms and strategies for light-assisted ferroelectric control shown here will stimulate further fundamental research and open new avenues for the design of novel optoferroic devices.

Methods

Effective Hamiltonian A novel effective Hamiltonian (H_{eff}) is developed for such material. It has the following degrees of freedom: vectors related to the ferroelectric soft mode (\mathbf{P}), high-frequency auxiliary mode (\mathbf{Q}) and inhomogeneous strain (\mathbf{u}) in each 5-atom unit cell, as well as, the homogenous strain (η). Both \mathbf{P} and \mathbf{Q} modes are infrared-active modes and can couple to external electric fields (via an energy involving a dot product with such field). Their associated local vectors in the H_{eff} are centered on Nb ions. In the KNbO₃ cubic structure, the

zone-center \mathbf{P} mode is soft (in the sense that the square of its frequency is negative at 0 K) while the \mathbf{Q} mode is also located at the zone center but possesses a high and positive frequency. The details of the mode frequency and eigenvector for both \mathbf{P} and \mathbf{Q} can be found in Sec. I of SM. The local vectors corresponding to the inhomogeneous strains are technically centered on K ions. The homogenous strain is defined with respect to cubic symmetry and has six independent components η_i in Voigt notation.

The potential energy U^{tot} of H_{eff} has four main contributions:

$$\begin{aligned} U^{tot} = & U^{FE}(\{\mathbf{P}\}, \{\mathbf{u}\}, \{\eta\}) \\ & + U^{aux}(\{\mathbf{Q}\}, \{\mathbf{u}\}, \{\eta\}) \\ & + U^{int}(\{\mathbf{P}\}, \{\mathbf{Q}\}) \\ & + U^{elastic}(\{\eta\}) \end{aligned} \quad (1)$$

a purely elastic one $U^{elastic}$; a second one related to the ferroelectric soft mode and its interaction with strains $U^{elastic}$, exactly like in Ref.⁴⁷ for BaTiO₃; a third one related to the high-frequency auxiliary mode and its interaction with strains U^{aux} , which has the same analytical form than the second energy but when replacing \mathbf{P} by \mathbf{Q} ; and a fourth one that gathers the direct interactions between the ferroelectric soft mode and high-frequency auxiliary mode U^{int} , and which are indicated in Table I. The details of all these four energies can be found in Section II of SM.

Such effective Hamiltonian is generated with respect to cubic (C) symmetry and can be involved in phase transitions among sub-group ferroelectric structures, such as tetragonal (T), orthorhombic (O), and rhombohedral (R) phases. Note that this new effective Hamiltonian resolves symmetry-broken issues expressed in previous works^{29,38,40}, and contains for the first time all the symmetry-allowed forms within fourth order. In addition, for the first time too, the model includes the full spatial degree of freedoms of both \mathbf{P} and \mathbf{Q} , i.e., their Cartesian components along x, y and z axes (which are along the three $<001>$ pseudo-cubic directions). The existence of these Cartesian components (P_x, P_y, P_z) and (Q_x, Q_y, Q_z) can, e.g., allow the ferroelectric polarization to rotate (and not “only” reverse its direction) when the \mathbf{Q} mode is activated. The model parameters of the H_{eff} are first determined from 0 K first-principle calculations but then a few of them are adjusted, in order to better agree with measurements but also to allow the calculations to converge (large coupling coefficients can result in simulations going towards infinite energy). This is why, for instance, the coefficient in front of (the third-order-in-P) $P_x^3 Q_x + P_y^3 Q_y + P_z^3 Q_z$ and (the complex) $P_x^2 P_y Q_y + P_x P_y^2 Q_x + P_x^2 P_z Q_z + P_x P_z^2 Q_x + P_y^2 P_z Q_z + P_y P_z^2 Q_y$ have been reduced from its *ab-initio* value or why the coefficient

in front of $P_x P_y Q_x Q_y + P_y P_z Q_y Q_z + P_z P_x Q_z Q_x$ has been modified (to give correct A and E mode splitting hierarchy, see supplementary material fig. 2). Note also that determining such coupling coefficients from first principles is not a unique and easy procedure and thus large error bars can be assigned to these coefficients. It is thus not surprising that they then require to be adjusted to allow for a better comparison with observations.

Moreover, the kinetic energy K^{tot} of the H_{eff} contains three parts written with respect to the velocity \mathbf{v}_p , \mathbf{v}_q , and \mathbf{v}_u that correspond to the order parameters, \mathbf{P} , \mathbf{Q} , and \mathbf{u} :

$$K^{tot} = \sum_i^N \frac{1}{2} M_p v_{p,i}^2 + \frac{1}{2} M_q v_{q,i}^2 + \frac{1}{2} M_u v_{u,i}^2 \quad (2)$$

where the effective masses are defined as M_p , M_q , and M_u respectively. Their values are fitted to produce the TO mode frequencies as calculated from the DFT phonon frequencies of the rhombohedral phase at zero K⁵⁷, and are listed in Table I of the SM.

Dynamic Simulations We employed Monte Carlo (MC) and Molecular Dynamic (MD) algorithms on a $12 \times 12 \times 12$ supercell that contains 8640 atoms. More specifically, we used parallel tempering^{58,59} (PT) MC and Nosé-Hoover thermal state⁶⁰⁻⁶² MD simulations implemented in LINVARIANT⁶³. The same Nosé mass for \mathbf{P} , \mathbf{Q} , and inhomogeneous strains of 10000 a.u. is used. The Nosé mass for the homogenous strains is 1 a.u. in all the simulations. Periodic boundary conditions were adapted. For each temperature, 150,000 PTMC sweeps are firstly performed, with the first 100,000 steps as thermalization and the subsequent 50,000 steps to compute the phase diagram; then MD simulations are initialized with the MC outputs and 500,000 thermalization steps are performed before the statistical evaluations; the time interval of 0.1fs is used in the MD simulations.

Data availability.

The authors declare that the coefficient data of the effective Hamiltonian are available within the paper and its supplementary Material; The data that support the findings of this study are available from the corresponding author upon reasonable request.

Code availability.

The code that generates and solves the effective Hamiltonian is available at <https://github.com/PaulChern/LINVARIANT>.

References

1. de la Torre, A. et al. Nonthermal pathways to ultrafast control in quantum materials. *arXiv* 2103.14888v1 (2021).
2. Rudner, M. S. & Lindner, N. H. Band structure engineering and non-equilibrium dynamics in floquet topological insulators. *Nat. Rev. Phys.* **2**, 229–244 (2020).
3. Mitrano, M. & Wang, Y. Probing light-driven quantum materials with ultrafast resonant inelastic x-ray scattering. *Commun. Phys.* **3**, 184 (2020).
4. Buzzi, M., Först, M., Mankowsky, R. & Cavalleri, A. Probing dynamics in quantum materials with femtosecond x-rays. *Nat. Rev. Phys.* **3**, 299–311 (2018).
5. Giannetti, C. et al. Ultrafast optical spectroscopy of strongly correlated materials and high-temperature superconductors: a non-equilibrium approach. *Adv. Phys.* **65**, 58–238 (2016).
6. Zhang, J. & Averitt, R. Dynamics and control in complex transition metal oxides. *Annu. Rev. Mater. Res.* **44**, 19–43 (2014).
7. Rini, M. et al. Control of the electronic phase of a magnetite by mode-selective vibrational excitation. *Nature* **449**, 72–74 (2007).
8. Caviglia, A. D. et al. Ultrafast strain engineering in complex oxide heterostructures. *Phys. Rev. Lett.* **108**, 136801 (2012).
9. Disa, A. S. et al. Polarizing an antiferromagnet by optical engineering of the crystal field. *Nat. Phys.* **16**, 937–941 (2020).
10. Först, M. et al. Spatially resolved ultrafast magnetic dynamics initiated at a complex oxide heterointerface. *Nat. Mater.* **14**, 883–888 (2015).
11. Lambert, C.-H. et al. All-optical control of ferromagnetic thin films and nanostructures. *Science* **345**, 1337–1340 (2014).
12. Manz, S. et al. Reversible optical switching of antiferromagnetism in TbMnO₃. *Nat. Photonics* **10**, 653–656 (2016).
13. Stanciu, C. et al. All-optical magnetic recording with circularly polarized light. *Phys. Rev. Lett.* **99**, 047601 (2007).
14. Prosandeev, S., Grollier, J., Talbayev, D., Dkhil, B. & Bellaiche, L. Ultrafast neuromorphic dynamics using hidden phases in the prototype of relaxor ferroelectrics. *Phys. Rev. Lett.* **126**, 027602 (2021).
15. Nova, T. F., Disa, A. S., Fechner, M. & Cavalleri, A. Metastable ferroelectricity in optically strained SrTiO₃. *Science* **364**, 1075–1079 (2019).
16. Li, J., Strand, H. U., Werner, P. & Eckstein, M. Theory of photoinduced ultrafast switching to a spin-orbital ordered hidden phase. *Nat. Commun.* **9**, 1–7 (2018).
17. Stojchevska, L. et al. Ultrafast switching to a stable hidden quantum state in an electronic crystal. *Science* **344**, 177–180 (2014).
18. Budden, M. et al. Evidence for metastable photo-induced superconductivity in K₃C₆₀. *Nat. Phys.* **17**, 611–618 (2021).
19. Fausti, D. et al. Light-induced superconductivity in a stripe-ordered cuprate. *Science* **331**, 189–191 (2011).
20. Kennes, D. M., Wilner, E. Y., Reichman, D. R. & Millis, A. J. Transient superconductivity from electronic squeezing of optically pumped phonons. *Nat. Phys.* **13**, 479–483 (2017).
21. Mitrano, M. et al. Possible light-induced superconductivity in K₃C₆₀ at high temperature. *Nature* **530**, 461–464 (2016).
22. McIver, J. W. et al. Light-induced anomalous hall effect in graphene. *Nat. Phys.* **16**, 38–41 (2019).
23. Sie, E. J. et al. An ultrafast symmetry switch in a weyl semimetal. *Nature* **565**, 61–66 (2019).
24. Wang, Y. H., Steinberg, H., Jarillo-Herrero, P. & Gedik, N. Observation of floquet-bloch states on the surface of a topological insulator. *Science* **342**, 453–457 (2013).
25. Guo, J. et al. Recent progress in optical control of ferroelectric polarization. *Adv. Opt. Mater.* 2002146 (2021).
26. Bilyk, V. et al. Transient polarization reversal using an intense THz pulse in silicon-doped lead germanate. *pss (RRL)* **15**, 2000460 (2020).
27. Yang, M.-M. & Alexe, M. Light-induced reversible control of ferroelectric polarization in BiFeO₃. *Adv. Mater.* **30**, 1704908 (2018).
28. Li, T. et al. Optical control of polarization in ferroelectric heterostructures. *Nat. Commun.* **9**, 3344 (2018).
29. Mankowsky, R., von Hoegen, A., Först, M. & Cavalleri, A. Ultrafast reversal of the ferroelectric polarization. *Phys. Rev. Lett.* **118**, 197601 (2017).
30. Grishunin, K. A. et al. THz electric field-induced second harmonic generation in inorganic ferroelectric. *Sci. Rep.* **15** (2017).
31. Morimoto, T. et al. Terahertz-field-induced large macroscopic polarization and domain-wall dynamics in an organic molecular dielectric. *Phys. Rev. Lett.* **118** (2017).
32. Chen, F. et al. Ultrafast terahertz-field-driven ionic response in ferroelectric BaTiO₃. *Phys. Rev. B* **94**, 180104(R) (2016).
33. Grübel, S. et al. Ultrafast x-ray diffraction of a ferroelectric soft mode driven by broadband terahertz pulses (2016). 1602.05435.
34. Rana, D. S. et al. Understanding the nature of ultrafast polarization dynamics of ferroelectric memory in the multiferroic BiFeO₃. *Adv. Mater.* **21**, 2881–2885 (2009).
35. Scott, J. F. & de Araujo, C. A. P. Ferroelectric memories. *Science* **246**, 1400–1405 (1989).
36. Guo, R. et al. Non-volatile memory based on the ferroelectric photovoltaic effect. *Nat. Commun.* **4**, 1990 (2013).
37. Först, M. et al. Nonlinear phononics as an ultrafast route to lattice control. *Nat. Phys.* **7**, 854–856 (2011).
38. Subedi, A. Proposal for ultrafast switching of ferroelectrics using midinfrared pulses. *Phys. Rev. B* **92**, 214303 (2015).
39. Yi, H. T., Choi, T., Choi, S. G., Oh, Y. S. & Cheong, S.-W. Mechanism of the switchable photovoltaic effect in ferroelectric BiFeO₃. *Adv. Mater.* **23**, 3403–3407 (2011).
40. Mertelj, T. & Kabanov, V. Comment on “ultrafast reversal of the ferroelectric polarization”. *Phys. Rev. Lett.* **123**, 129701 (2019).
41. Zhong, W., Vanderbilt, D. & Rabe, K. M. First-principles theory of ferroelectric phase transitions for perovskites: The case of BaTiO₃. *Phys. Rev. B* **52**, 6301–6312 (1995).
42. Triebwasser, S. Behavior of ferroelectric KNbO₃ in the vicinity of the cubic-tetragonal transition. *Phys. Rev.* **101**, 993–997 (1956).
43. Hewat, A. W. Cubic-tetragonal-orthorhombic-rhombohedral ferroelectric transitions in perovskite

- 775 potassium niobate: neutron powder profile refinement
776 of the structures. *J. Phys. C: Solid State Phys.* **6**,
777 2559–2572 (1973).
- 778 44. Tinte, S., Íñiguez, J., Rabe, K. M. & Vanderbilt,
779 D. Quantitative analysis of the first-principles effective
780 hamiltonian approach to ferroelectric perovskites.
781 *Physical Review B* **67** (2003).
- 782 45. Krakauer, H., Yu, R., zhang Wang, C., Rabe, K. &
783 Waghmare, U. Dynamic local distortions in KNbO₃.
784 *J. Phys.: Condens. Matter* **11**, 3779–3787 (1999).
- 785 46. Xu, B., Íñiguez, J. & Bellaïche, L. Designing lead-free
786 antiferroelectrics for energy storage. *Nat. Commun.* **8**,
787 15682 (2017).
- 788 47. Zhong, W. & Vanderbilt, D. Competing structural insta-
789 bilities in cubic perovskites. *Phys. Rev. Lett.* **74**, 2587–
790 2590 (1995).
- 791 48. Sai, N. & Vanderbilt, D. First-principles study of ferro-
792 electric and antiferrodistortive instabilities in tetragonal
793 SrTiO₃. *Phys. Rev. B* **62**, 13942–13950 (2000).
- 794 49. Kornev, I. A., Bellaïche, L., Janolin, P.-E., Dkhil, B. &
795 Suard, E. Phase diagram of Pb(zr, ti)o₃ solid solutions
796 from first principles. *Phys. Rev. Lett.* **97** (2006).
- 797 50. Gu, T. et al. Cooperative couplings between octahedral
798 rotations and ferroelectricity in perovskites and related
799 materials. *Phys. Rev. Lett.* **120** (2018).
- 800 51. Steigerwald, H. et al. Direct writing of ferroelectric do-
801 mains on the x- and y-faces of lithium niobate using a
802 continuous wave ultraviolet laser. *Appl. Phys. Lett.* **98**,
803 062902 (2011).
- 804 52. Boes, A. et al. Direct writing of ferroelectric domains on
805 strontium barium niobate crystals using focused ultravio-
806 let laser light. *Appl. Phys. Lett.* **103**, 142904 (2013).
- 807 53. Hadni, A. & Thomas, R. Localized irreversible thermal
808 switching in ferroelectric TGS by an argon laser.
809 *Ferroelectrics* **6**, 241–245 (1973).
- 810 54. Abalmasov, V. A. Ultrafast reversal of the ferroelectric
811 polarization by a midinfrared pulse. *Phys. Rev. B* **101**
812 (2020).
- 813 55. Martin, S., Baboux, N., Albertini, D. & Gautier, B.
814 A new technique based on current measurement for
815 nanoscale ferroelectricity assessment: Nano-positive up
816 negative down. *Rev. Sci. Instrum.* **88**, 023901 (2017).
- 817 56. Qi, T., Shin, Y.-H., Yeh, K.-L., Nelson, K. A. & Rappe,
818 A. M. Collective coherent control: Synchronization of
819 polarization in FerroelectricPbTiO₃by shaped THz fields.
820 *Phys. Rev. Lett.* **102** (2009).
- 821 57. Wang, C.-Z., Yu, R. & Krakauer, H. Polarization de-
822 pendence of born effective charge and dielectric constant
823 inKNbO₃. *Phys. Rev. B* **54**, 11161–11168 (1996).
- 824 58. Hukushima, K. & Nemoto, K. Exchange monte
825 carlo method and application to spin glass simulations.
826 *J. Phys. Soc. Jpn.* **65**, 1604–1608 (1996).
- 827 59. Katzgraber, H. G., Trebst, S., Huse, D. A. & Troyer,
828 M. Feedback-optimized parallel tempering monte
829 carlo. *J. Stat. Mech: Theory Exp.* **2006**, P03018–P03018
830 (2006).
- 831 60. Nosé, S. A molecular dynamics method for simulations in
832 the canonical ensemble. *Mol. Phys.* **52**, 255–268 (1984).
- 833 61. Nosé, S. A unified formulation of the constant temper-
834 ature molecular dynamics methods. *J. Chem. Phys.* **81**,
835 511–519 (1984).
- 836 62. Hoover, W. G. Canonical dynamics: Equilibrium phase-
837 space distributions. *Phys. Rev. A* **31**, 1695–1697 (1985).
- 838 63. Chen, P., Zhao, H., Artyukhin, S. & Bellaïche,
839 L. LINVARIANT. [https://github.com/PaulChern/
840 LINVARIANT](https://github.com/PaulChern/LINVARIANT) (2019).
- 841 **Acknowledgements**
- 842 The work is supported by ONR under Grant No.
843 N00014-17-1-2818 (P.C. and L.B.), the Vannevar Bush
844 Faculty Fellowship (VBFF) grant no. N00014-20-1-2834
845 from the Department of Defense (H.J.Z and L.B.) and
846 the ARO Grant No. W911NF-21-1-0113. (L.B.). C.P.
847 thanks the support from a public grant overseen by the
848 French National Research Agency (ANR) as part of the
849 “Investissements d’Avenir” program (Labex NanoSaclay,
850 reference: ANR-10-LABX-0035). J.Í. is funded by the
851 Luxembourg National Research Fund through Grant
852 FNR/C18/MS/12705883/REFOX. The simulations of
853 effective Hamiltonian and density functional theory were
854 done using the Arkansas High Performance Computing
855 Center.
- 856
- 857 **Author contributions**
- 858 L.B. and J.I. conceived the work; P.C., C.P. and L.B.
859 implemented the effective Hamiltonian and performed
860 numerical simulations; P.C., H.J.Z. and L.B. carried out
861 the analysis and explanation of the data; all authors
862 participated in the discussion and preparation of this
863 work.
- 864
- 865 **Competing interests**
- 866 The authors declare no competing interests.